Experimental and numerical studies on the frame-infill in-teraction in steel reinforced recycled concrete frames

Jianyang Xue[*], Xiaogang Huang, Zheng Luo and Liang Gao

College of Civil Engineering, Xi'an University of Architecture and Technology, Xi'an, P.R. China

Abstract.   Masonry infill has a significant effect on stiffness contribution, strength and ductility of masonry-infilled frames. These effects may cause damage of weak floor, torsional damage or short-column failure in structures. This article presents experiments of 1/2.5-scale steel reinforced recycled aggregates concrete (SRRC) frames. Three specimens, with different infill rates consisted of recycled concrete hollow bricks (RCB), were subjected to static cyclic loads. Test phenomena, hysteretic curves and stiffness degradation of the composite structure were analyzed. Furthermore, effects of axial load ratio, aspect ratio, infill thickness and steel ratio on the share of horizontal force supported by the frame and the infill were obtained in the numerical example.

Keywords: steel reinforced recycled aggregates concrete; infilled frames; frame-infill interaction; shear distribution; axial load ratio; aspect ratio; infill thickness; steel ratio

1. Introduction

The amount of construction and demolition waste is estimated at billions of tons per year with an increasing trend. The importance of environmental considerations in the field of structures has triggered many researches on construction and demolition waste. Nevertheless, in comparison with natural aggregates, recycled concrete and blocks with a high waste composition show differences in main mechanical, deformability and durability properties (Otsuki *et al*. 2003, Xiao 2008, Gomes and de Brito 2009). The test results by Poon *et al*. (2002) showed that replacement of coarse and fine natural aggregates by recycled aggregates at the levels of 25% and 50% had little effect on the compressive strength of brick and block specimens, but higher levels of replacement reduced the compressive strength. Etxeberria *et al*. (2007) used four different recycled aggregate concretes to examine the difficulty of obtaining the same high compressive strength in concrete with high percentages of recycled aggregates and conventional concrete.

Then some researchers performed a series of experiments to analyze the mechanical performance of RAC in view of the advantages of steel-reinforced concrete structures. Ma *et al*. (2013) found that the seismic performance of SRRC columns decreased slightly as the RCA replacement percentage increases. The results also indicated that appropriate design of the axial compression ratio could improve the seismic performance of SRRC columns. Research by Xue *et*

---

*Corresponding author, Professor, Ph.D., E-mail: jianyang_xue@163.com

al. (2014) also showed that the shear resistance, energy dissipation capacity and ductility of SRRC innerframe joints kept little change with respect to regular joints. Parametric analysis by Liu *et al*. (2015) indicated that normal cross-section bearing capacity of SRRC columns could be changed in varying degrees under the influence of concrete strength grade, steel strength, steel ratio, and loading angle, but it made little difference for normal cross-section bearing capacity of SRRC columns ranging from 0% to 100% of aggregate replacement subjected to quasi-static reversed cyclic loading. So the use of steel in the column could obviously improve the mechanical performance of SRRC columns adopting high recycled aggregates ratios.

On the basis of the aforementioned research results, the SRRC columns and inner-frame joints show good seismic performance However, there has been no research on the seismic performance of steel reinforced concrete structures with RAC. Many researches have shown that the infill can completely change the distribution of damage throughout the masonry-RC frames (Dolšek and Fajfar 2008, Pujol and Fick 2010, Tasnimi and Mohebkhah 2011, Agrawal and Hora 2012, Cavaleri and Di Trapani 2014). The main objective of the study described in this paper is to analyze shear resistance of SRRC frames with infill walls which consist of recycled concrete hollow bricks (RCB). The composite structure could maximize the consumption of the recycled mixed aggregates. This paper presents our experimental investigation on the 1/2.5-scale, one story, one bay, recycled masonry-infilled SRRC frame. A comparison test has been made on the behavior of the bare SRRC frame. The effects of axial load ratio, aspect ratio, infill thickness and steel ratio on the composite structure were analyzed by Perform-3d program with discussion of shear distribution of both frame portion and masonry portion.

2. Experimental work

2.1 Description of test specimens

In order to study the degree of coupling between SRRC frame and infill consisted of RCB, three 1/2.5-scale single-story, single-bay specimens made with 100% coarse recycled aggregate were fabricated. The geometric dimensions and reinforcement layout of the test specimens are shown in Figs. 1(a)-(d). One frame was tested without an infill panel (S1), one had a full-height infill panel (S2), and another had half-height infill panel. Geometrical dimensions and reinforcement of all specimen frames were selected to be the same. RCB units with a dimension of 390 mm × 190 mm × 90 mm and 26% hollow ratio were used in masonry wall as described in Fig. 1(e). The thickness of 1/2.5-scale infill wall is 90 mm. Connection between the frame and the infill was achieved by using 6-mm diameter horizontal reinforcements placed in holes drilled into inner faces of the columns.

Grade Q235B steels were used as steel skeleton in columns using I14 sections (A = 21.5 cm^2, I_x = 712 cm^4, h = 14 cm, b = 8 cm, t_f = 0.91 cm, t_w = 0.55 cm). Φ14 bars were used as the longitudinal steel bars in columns and beams. ϕ6 bars and Φ8 bars were used as stirrups in the beams and the columns, respectively. The average steel ratio and reinforcement ratio of the column were 4.98% and 1.43%, respectively. In the 455 mm range of each column end and the whole joints zone, the stirrups were arranged at 50 mm interval, and in other parts of the column, the stirrups were arranged at 100 mm interval. Columns were supported by 3720 mm × 500 mm × 500 mm footing fastened to the strong floor at State Key Laboratory of Science and Technology in Western China. As drawn in Fig. 2, longitudinal bars on the edge of the beam got through steel

(a) S1 geometry   (b) S2 geometry   (c) S3 geometry

(d) Reinforcement details of columns and beams   (e) RCB employed to arrange infills
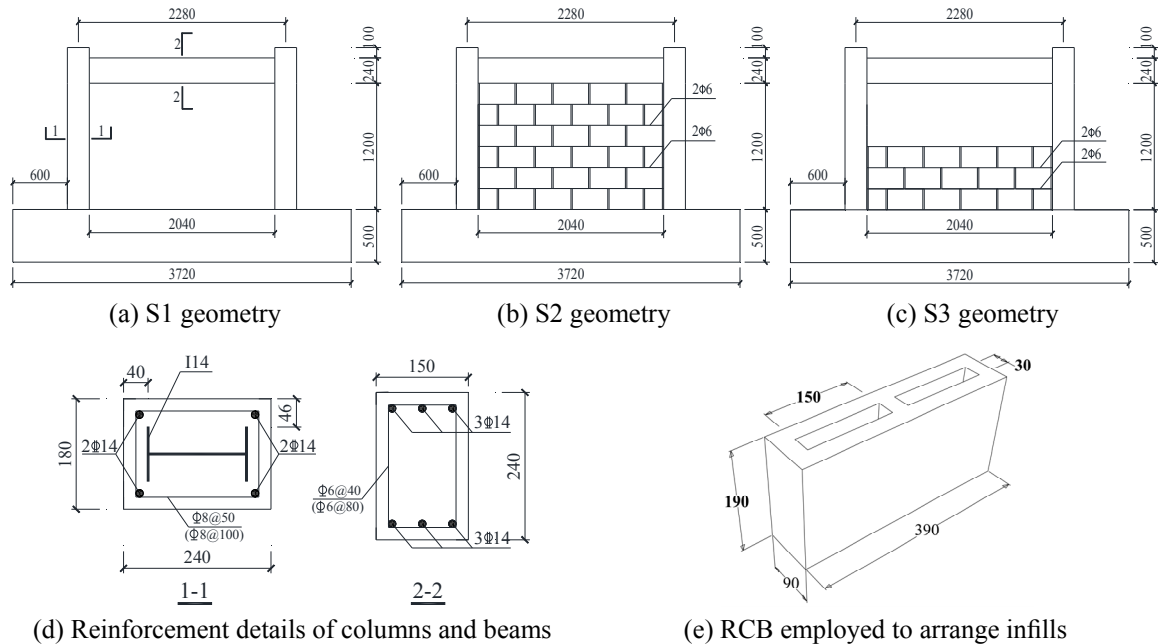
Fig. 1 Specimen geometry and reinforcement details (mm)

flange plate in the columns and extended to joints zone according to GB50010-2010. In the 500mm range of each beam, the stirrups were arranged at 40 mm intervals, and in other parts of the beam, the stirrups were arranged at 80 mm intervals. The longitudinal bar in the middle of the beam is connected by fillet weld with connection plate welded in the steel.

2.2 Test setup and instrumentation

The test was designed to study properties related to the failure modes, strength and displacement capacity of SRRC frames. The load was applied by two hydraulic jacks on top of each column of the test specimen before lateral loads were applied. The design value of axial load ratio for the two columns was 0.4. Cyclic lateral loads were applied by one horizontal actuator. The actuator attached to the beam end was operated in load-displacement hybrid control in which the lateral loading sequence was controlled by force for the initial loading cycles till the yielding initiation of the test specimen was observed. Starting from 30 kN, every load level was applied for one cycle at an increment of 30 kN. When the specimen started yielding, the loading sequence was controlled by displacement. On basis of the yield displacement, the target displacements for the cyclic loading were set as the multiple of the yield displacement, the cyclic loadings were repeated three times at each target displacement. Loading was terminated until the reaction force descended to about 85% of the maximum value.

The specimens were instrumented with several strain gauges and displacement meters to measure the parameters characterizing the structural response of the frame and the infill walls. The parameters included horizontal deformation of the columns at 330 mm equal spacing, strains at the distance of 100 mm, 300 mm and 500 mm from beam end, and strains at the distance of 100 mm and 400 mm from column end. All the data were collected by TDS-602 static data acquisition
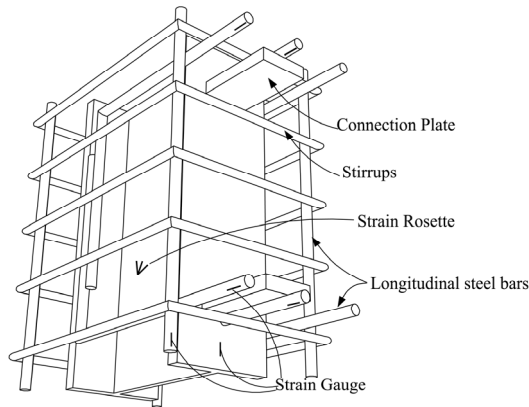
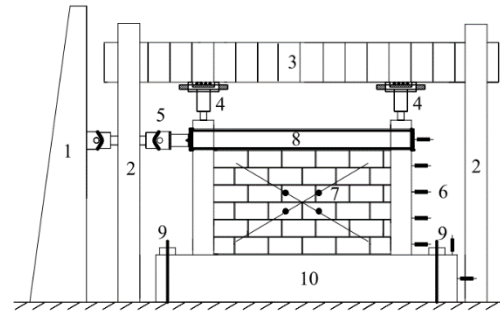Fig. 2 Schematic of lap splice and gauge points

Fig. 3 Test setup

Table 1 Mix proportions of RAC (kg/m^3)

Replacement ratios	W/C	Cement	Sand	Recycled coarse aggregate	Water	Water-reducing agent
100%	0.42	488	527	1158	205	5

instrument. Strain gauges attached to bars and steel near joints are shown in Fig. 2. The test setup, including the loading system, specimen and displacement meters is shown in Fig. 3 (1 - reaction wall; 2 - reaction steel frame; 3 - reaction girder; 4 - vertical actuator; 5 - 1000 kN horizontal actuator; 6 - displacement meter; 7 - dial indicator; 8 - horizontal braces; 9 - tie bolt; 10 - footing).

2.3 Material

The material designated as concrete rubble was obtained from the demolition of concrete prefabricated components crushed by a jaw crusher, with a compression strength class of C20 and a maximum dimension of aggregate of 30 mm. The mix proportions of recycled aggregate concrete are shown in Table 1, where W/C stands for water/cement ratio. The compressive strength and unit weight of hardened concrete mixtures were determined on three 150 mm cube specimens, which were prepared in the similar manner in the laboratory. Masonry infill walls were constructed 7 days after completion of SRRC frame. The measured average compressive and tensile strength of brick samples were 5.62 MPa and 2.7 MPa, respectively. The mortar mixture consists of cement, sand and water with a ratio of 1:5:1. Three mortar 70.7 mm cube specimens were tested for compressive strength according to Code JGJ/T70-2009. Mortar average strength was measured to 10.11 MPa. I14, Φ6, Φ8 and Φ14 had a yield stress of 286.9 MPa, 415.7 MPa, 508.6 MPa and 494.1 MPa, respectively.

3. Experimental phenomenon

3.1 Specimen S1

Vertical flexural cracks at the beam ends were firstly observed under a loading of ±60 kN. As the lateral loading increased, more flexural cracks occurred and developed at beam ends. Under

the loading of ±100 kN, many new cracks occurred far away from beam ends. Under the loading of ±140 kN, horizontal cracks occurred at the column bottoms and the length of cracks at the beam end increased. Under the loading of ±180 kN, some major flexural cracks formed at the beam ends and the crack length at the column bottoms increased. Under the loading of ±240 kN, successive cracks formed at the beam ends and the column bottoms and the maximum width of cracks in the column bottom was about 1mm. At ±25 mm displacement, a small amount of concrete dropped at the beam ends and the column bottoms, and the maximum width of the flexural cracks was about 2 mm. At ±33 mm displacement, a large amount of concrete crushed and dropped at the beam ends. At ±42 mm displacement, a large amount of concrete crushed and dropped at the column bottoms. At ±59 mm displacement, concrete spalling at the beam ends grew continuously, and the stirrups and longitudinal steel bars were exposed. At ±68mm displacement, the horizontal web steel yielded and massive concrete exfoliation were observed at the column bottoms at last. The failure mode of S1 is shown in Fig. 4(a).

3.2 Specimen S2

Separations between the bounding frame and the infill corner and fine cracks in the masonry were firstly observed under the horizontal loading of ±120 kN. Under the loading of ±150 kN, fine vertical and horizontal cracks occurred at beam ends and column bottoms, respectively and more approximately 45° cracks occurred and developed at the corner of the wall. Under the loading of ±180 kN, the initial diagonal cracks at the top corner of the wall began developing to the mid-height of the wall. Under the loading of ±210 kN, flexural cracks in the beam ends and the column bottoms widened and the initiated diagonal cracks went through the bricks. Under the loading of ±300 kN, separations between the wall and the bounding frame were visible apparently, and fine diagonal cracks occurred at beam end. Under the loading of ±390 kN, these approximately 45° cracks joined the horizontal cracks that developed along the mortar joints near the mid-height of the wall and the beam ends and column bottoms experienced successive cracking in the form of horizontal and vertical cracks. Under the loading of ±420 kN, several main sliding cracks were observed along the horizontal mortar joint. At ±10 mm displacement, the length of cracks at the beam ends and the column bottoms were observed to increase and additional cracks developed along the vertical mortar joints at the wall corner. At ±20 mm displacement, holes occurred at upper corners and mid-height of the wall, concrete crushed and dropped at the beam ends and the column bottoms, and vertical cracks at the beam became wider. The failure mode of S2 is shown in Fig. 4(b).

3.3 Specimen S3

Separations between the columns and the partial infill were firstly observed under the horizontal loading of ±60 kN. Under the loading of ±90 kN, fine vertical cracks initiated at beam ends. As the lateral loading increasing, more flexural cracks were observed occurring and developing at beam ends, and diagonal cracks went through bricks at the corner. Under the loading of ±210 kN, the main sliding cracks were observed along the horizontal mortar joint and separations between the columns and the infill was visible apparently. At ±33 mm displacement, crushing of the infill occurred near the sides. At a larger displacement, concrete crushed and dropped earlier at the beam ends than column bottoms. At ±68 mm displacement, massive exfoliations were observed at the beam ends and the infill corner at last. The failure mode of S3 is shown in Fig. 4(c).
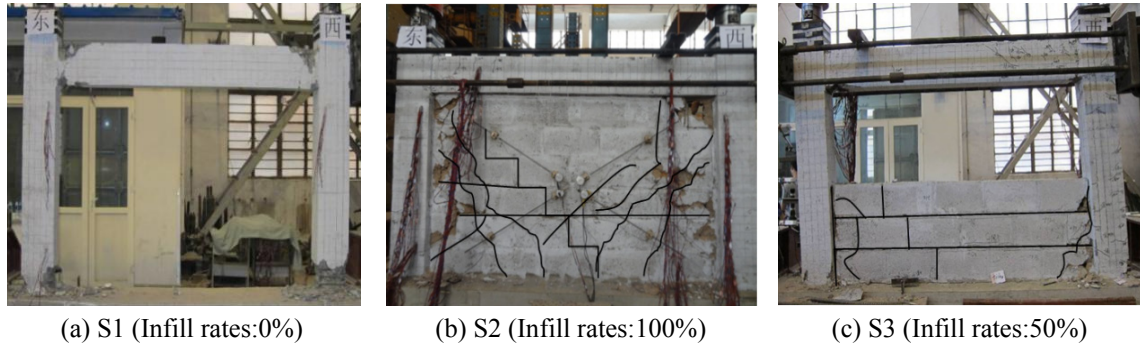
(a) S1 (Infill rates:0%)   (b) S2 (Infill rates:100%)   (c) S3 (Infill rates:50%)

Fig. 4 Failure modes of specimens

4. Discussion of test results

4.1 Hysteresis loops and skeleton curves

Figs. 5 and 6 show the relationship between lateral load (P) and displacement (Δ) during the test. The infill rates have a significant impact on load-displacement response. The hysteretic curves of S2 and S3 become pinching with respect to S1 because the shear-sliding cracks were developed in the infill. The bearing capacity of S2 descends obviously after the peak load is reached. A significant loss of strength is observed after a drift of 1.2% and then the hysteresis loops are in
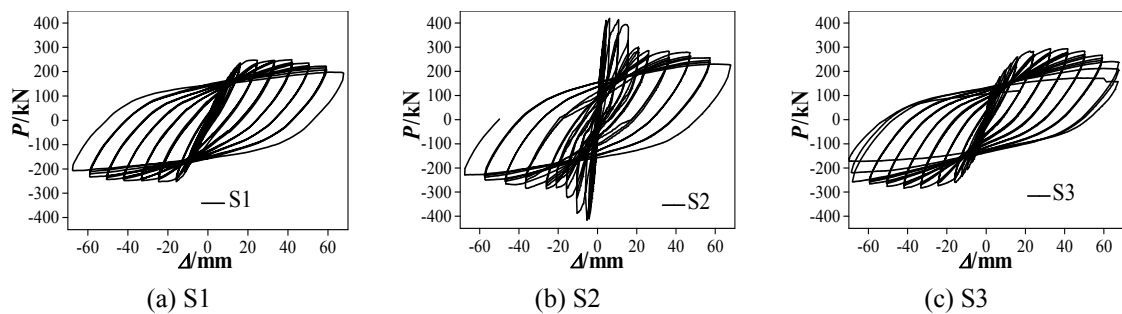

(a) S1   (b) S2   (c) S3

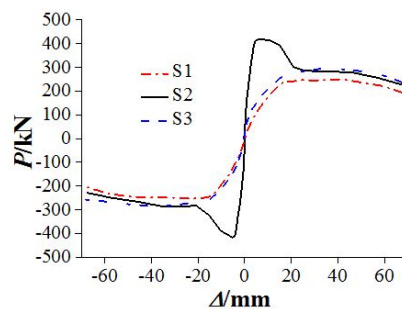Fig. 5 Load–displacement relations for S1, S2 and S3

Fig. 6 Comparison of skeleton curves from the test

spindle shape similar to the bare frame. Damage happens slightly at the beams and columns of S2 when the horizontal loading value drops to 85% peak value because of the beneficial effects of the infill. Then lateral load is borne by the frame portion of S2 after the failure of diagonal compression strut mechanism of masonry portion. The solid infill increases the initial stiffness and the maximum strength of S2 by approximately 12.60 times and 1.75 times, respectively. The partial infill of S3 cannot play a role in passive energy dissipation because of premature separations between the frame and the infill, which increases the initial stiffness of S3 by approximately 2 times. There is little difference in the hysteretic curves of S1 and S3.

4.2 Stiffness degradation

The bearing capacity and roof drift obtained from the test are shown in Table 2. As seen from this table, the bearing capacities and displacement in positive and negative direction of the test specimens are approximately the same. Here, P_y stands for the yield load, which is calculated by the method of universal yield moment (Lubliner 2006). P_m stands for the peak load, and P_u stands for the failure load. Δ_y, Δ_m and Δ_u are displacements corresponding to load P_y, P_m and P_u, respectively. θ_y, θ_m and θ_u are the roof drift respectively corresponding to the load P_y, P_m and P_u. The mean roof drift ratio of S2 at failure point is 331% smaller than the one calculated from S1 and the mean failure load of S2 is 40.3% larger than that of S1.

The stiffness degradation of S1, S2 and S3 under different loading levels is provided in Fig. 7, which reflects the degradation of the resistance of lateral collapse. From this figure, the initial stiffness in positive and negative direction of the test specimens is similar, and the extent of

Table 2 Experiment results at main loading stages (θ = Roof drift/height)

| Specimen	Loading direction	Yield point			Peak point			Failure point		
		P_y /kN	Δ_y /mm	θ_y	P_m /kN	Δ_m /mm	θ_m	P_u /kN	Δ_u /mm	θ_u
S1	Positive	175.19	9.94	1/133	246.62	24.72	1/53	209.63	62.97	1/21
	Negative	-180.00	-9.06	1/146	-252.47	-24.64	1/54	-214.6	-64.83	1/20
S2	Positive	286.82	2.32	1/569	419.09	6.10	1/216	356.23	16.84	1/78
	Negative	-280.45	-2.18	1/605	-416.71	-5.33	1/248	-354.2	-12.96	1/102
S3	Positive	210.90	10.31	1/128	294.12	32.69	1/40	250.00	60.25	1/22
	Negative	-220.77	-10.94	1/121	-283.46	-33.35	1/40	-240.9	-59.00	1/22

(a) S1   (b) S2   (c) S3
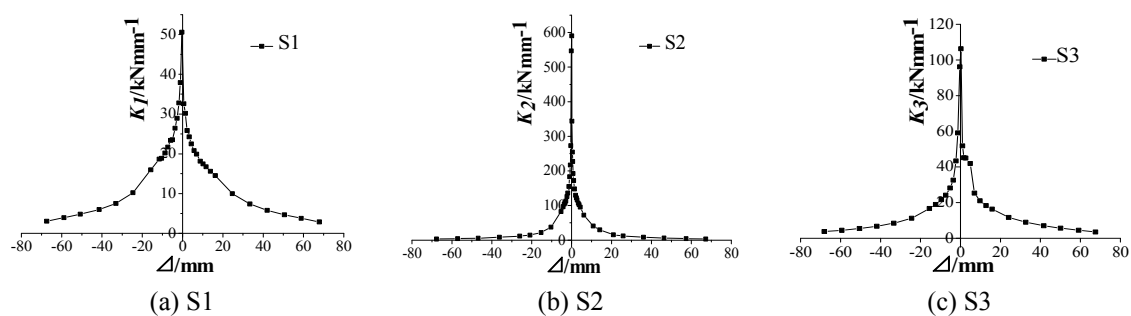
Fig. 7 Curves of stiffness degradation

stiffness degradation is symmetric. The masonry portion has large stiffness and poor deformation capacity at the early stage of loading, resulting in larger initial stiffness of S2. Then a lot of concrete cracks appear and concrete crush locally in the masonry which leads to fast stiffness degradation. With the development of plastic deformation, the stiffness degradation slows down gradually, indicating that lateral loads are mainly borne by the frame portion of S2 at this point. Therefore, the S2 still has a good inelastic deformation capacity after the failure point. The stiffness degradation of S3 is similar with that of S1.

5. Numerical studies

5.1 Models of SRRC frames

This paper employs general wall element for modelling of the masonry infill and fiber segments for modelling the nonlinear behavior of beams and columns. The reference structural model (Fig. 8) was formulated using Perform-3d software. The cross section of general wall element is a fiber section with 2 horizontal rebar fibers and 6 masonry wall fibers. Bricks and mortars in the numerical model are analyzed as a whole in the macro element (El-Dakhakhni *et al*. 2003, Asteris *et al*. 2011, Smyrou *et al*. 2011). Every masonry wall element consists of shear layer and diagonal compression layer acting in parallel to model shear behavior and diagonal strut action. Note that diagonal layers are intended mainly to model strut and tie action and shear layers assume constant shear stress and are based on the contribution of the mortar to the shear strength. The
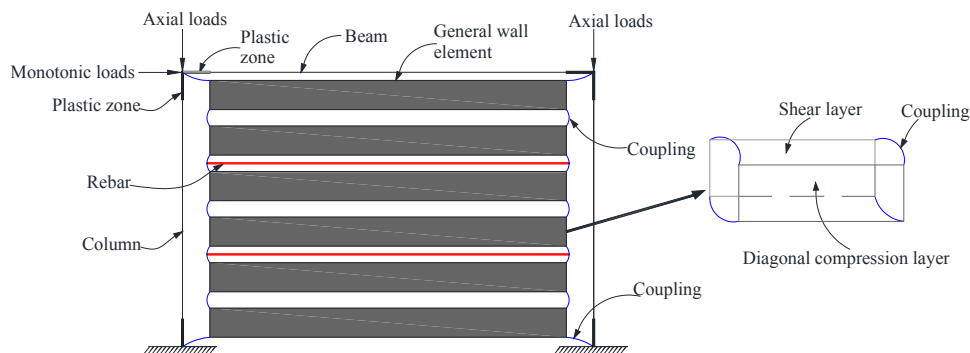

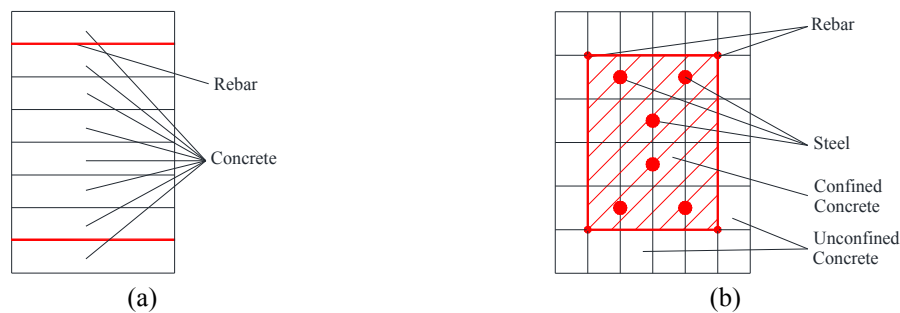Fig. 8 Structural model employed for the analyses

Fig. 9 Schematic of fiber cross sections for: (a) beams; and (b) columns

layers interact because they are connected at the nodes. The out-of-plane properties of the wall are defined as elastic. Also, 10 fibers are specified for the beam section which includes 2 rebar fibers and 8 concrete fibers, and 46 fibers are for the column section including 4 rebar fibers, 6 steel fibers and 36 concrete fibers based on area equivalence principle, as shown in Fig. 9. Based on the strain analysis, only the longitudinal bars and steel at the distance of 100 mm from beam end and column end yield. So the plastic zone length of beams and columns is defined as half of the depth of the cross section. Fiber models do not take into account shear mechanism because shear failures were not observed in the bounding frame during the test.

5.2 Constitutive models

The stress–strain relationships for the material used in the analyses are described in Fig. 10. Here, $K0$ stands for elasticity modulus, FY, FU and FR stand for yield strength, peak strength and residual strength, respectively, DU and DR stand for the strains correspond to FU and FR, respectively, DL stands for maximum ductile point. They have been implemented in the finite element program Perform-3d. The tension strength for concrete and bricks is specified as zero.
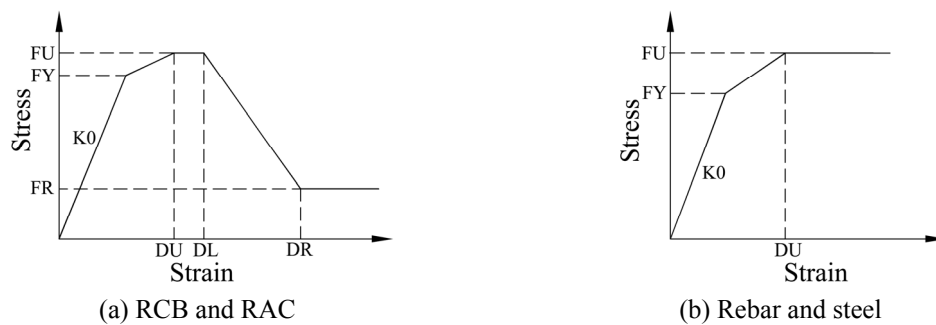

(a) RCB and RAC   (b) Rebar and steel

Fig. 10 The idealized stress–strain relationship for the material

(a) Prism subjected to axial load   (b) Sample subjected to shear load
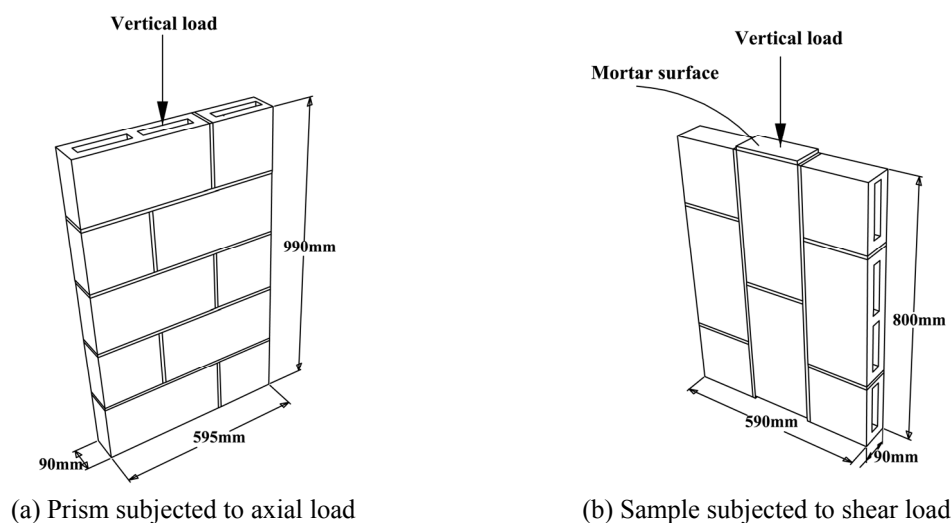
Fig. 11 General specimen schematics

Three 100 mm × 100 mm × 300 mm prism elements with a 100% recycled coarse aggregates were prepared in the similar manner in the laboratory in order to determine the material parameters chosen in the numerical analyses and test by electrohydraulic servo machine at the 28th day. The elasticity modulus of confined concrete is defined as the same as unconfined concrete. The other material properties of confined concrete are calculated using the Mander Confined Concrete Model (Mander *et al.* 1988) considering the constraint effect of stirrups in the columns. Modulus of elasticity is defined as values of the secant modulus of elasticity between stress 0% and 40% of the maximum stress. General specimen schematics are shown in Fig. 11.

The stress–strain relationships of masonry prism for inelastic compression were tested using electrohydraulic servo machine following Code GB/T50129-2011, which were computed on the basis of results of tests of six specimens subjected to axial load. Masonry prism had four mortar joints and five layers of bricks, each layer having 1.5 bricks. The peak strength *FU* was defined as maximum compressive strength of masonry prism measured according to Fig. 11(a). Other parameters of inelastic compression are calibrated to match the observed stiffness and strength of test results of S2. The strain *DU* corresponding to *FU*, the residual strain *DR* can be determined as shown in Eqs. (1)-(2).

$$DU = \frac{L_{\text{inf}}}{r_{\text{inf}}^2} \Delta_y \tag{1}$$

$$DR = \frac{L_{\text{inf}}}{r_{\text{inf}}^2} \Delta_{res} \tag{2}$$

Where L_{inf} represents length of infill panel; r_{inf} represents diagonal length of infill panel; Δ_y represents lateral drift corresponding to the peak strength of cyclic test of S2; Δ_{res} represents lateral drift corresponding to the residual strength of cyclic test of S2.

The stress–strain relationships of masonry prism for shear behavior were computed on the basis of results of tests of another six specimens subjected to shear load according to Fig. 11(b). The bricks in the shear component test were fabricated in accordance with construction method of

Table 3 Nonlinear material properties of RAC and masonry

Material	K0	FY	FU	FR	DU	DL	DR
	(MPa)						
Unconfined concrete	19200	34.47	38.30	5.75	0.0024	0.0026	0.0033
Confined concrete	19200	39.99	44.43	6.66	0.013	0.015	0.021
Inelastic compression for a wall	6120	3.24	3.6	0.54	0.0015	0.002	0.0075
Inelastic shear for a wall	2448	0.18	0.2	0.03	0.0002	0.00022	0.00033

Table 4 Nonlinear material properties of steel and rebar

Material	K0 (MPa)	FY (MPa)	FU (MPa)	DU
Q235 (I14)	2.08×105	286.9	413.3	0.08
HPB300 (Φ6)	2.66×105	415.7	534.9	0.08
HRB335 (Φ8)	1.99×105	508.6	659.7	0.08
HRB400 (Φ14)	2.02×105	494.1	665.7	0.08

masonry portion of S2 and S3. The peak strength *FU* and its corresponding strain *DU* were defined according to the material test under shear load. A ratio of 1.5 between *DR* and *DU* of inelastic shear for a wall was arbitrarily assumed because of abrupt failure in the test (Hashemi 2007).

Due to the lack of data and uncertainties in the modelling, it was necessary to arbitrarily assume several parameters for the mathematical model. In our model the yield strength of the infill was arbitrarily defined as 90% of peak strength and the residual strength of the infill was arbitrarily defined as 15% of peak strength in order to obtain a better correlation between the calculated and measured descent stage of load-displacement curves. The mean values of the specimens are shown in Table 3.

Material tests on steel and bars were also performed, and then the modulus of elasticity, yield strength, ultimate strength and ultimate strain were identified as shown in Table 4.

5.3 Numerical results

The load-displacement envelopes of S1 and S2 are plotted in Fig. 12 together with that of corresponding finite element model subjected to the monotonic loading. The experimental numerical analyses by Koutromanos and Stavridis suggest that the inelastic behavior of infilled frames is not very sensitive to the lateral loading history but a monotonically increasing load may lead to higher peak strength than fully reversed load cycles. Therefore, the monotonic loading is not considered to affect the validation of numerical results.

Fig. 12 shows an excellent agreement between the calculated and test results in ascent phase and peak strength, as well as descending phase, the close correspondence between numerical and experimental results lent strong support to the results of numerical model. However, the monotonic analyses give slightly larger peak strength. Also the results calculated with numerical method are 5.81% larger at the later stage of loading than the test ones.

As can be seen in Fig. 13, the load distribution between the frame portion and the masonry portion of S2 cannot be captured in the test, but the numerical analyses capture the load distribution between the frame portion and the masonry portion very well. From this figure, the skeleton curve of S1 is similar to that of the frame portion of S2 from the numerical analysis. Nevertheless, there is a big difference in stiffness and bearing capacity between the frame portion and the masonry portion. At the early stage of loading, the stiffness contribution of masonry portion for S2 is considerably larger than that of frame portion, which is close to total stiffness of
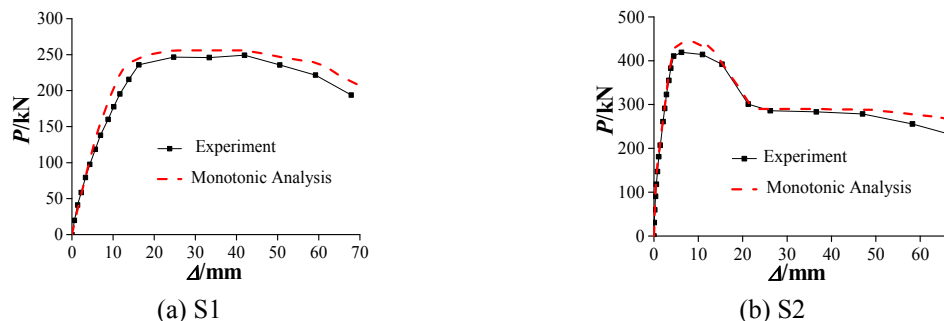

(a) S1   (b) S2

Fig. 12 Comparison of experimentally recorded and numerically obtained load-displacement curves for the frames
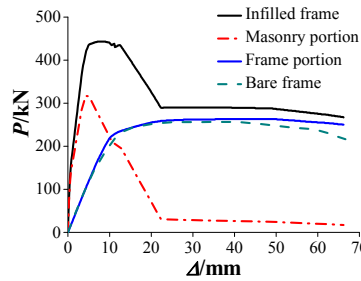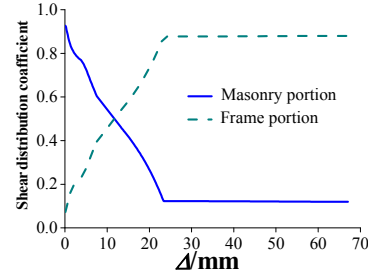
Fig. 13 *P*-Δ curve of different portions

Fig. 14 Shear distribution of frame portion
and masonry portion

S2. The frame portion is still in the elastic stage till the total peak load is reached, and then total bearing capacity begins to decline as the bearing capacity of the infill wall declines rapidly. With the perceptible and abrupt drops in bearing capacity of infill wall portion, the skeleton curve of S2 possesses an apparent descent trajectory, and then the descending branch is gentle. This indicates that the structure has good ductility. Fig. 14 shows the relationship between shear distribution coefficient and roof drift measured during the test of S2.

6. Parameter analysis

In terms of the effect on the seismic performance of infilled SRRC frames, there are many parameters that need to be considered. With the limitation of macro models, the effects of axial load ratio, aspect ratio, infill thickness and steel ratio on the share of horizontal force supported by the frame and the masonry wall without openings of infilled frame (IF) are analyzed respectively. The bare frame (BF) was calculated as reference frame.

6.1 Axial load ratio

In this part, the effects of axial load ratio on seismic response of SRRC frames are discussed by numerical analyses. The axial load ratio is defined as $n = N/(f_c A_c + f_{ss} A_{ss})$, where N stands for axial load, f_c and f_{ss} stand for concrete and steel design compressive strength, respectively. A_c and A_{ss} are the cross sectional areas corresponding to f_c and f_{ss}, respectively. The share of horizontal force of different portions of IF and *P*-Δ curve of BF and IF are given in Fig. 14 when axial load ratio is 0, 0.2, 0.4, 0.6 and 0.8 respectively.

Fig. 15 shows that, the initial stiffness and ductility of the frame portion is much better in comparison with BF with the increment of axial load ratio and the ultimate strength of BF calculated with numerical method is about 21% smaller than the ones of frame portion of IF when *n* is 0.8. This situation reveals the beneficial effects for improving mechanical performance of SRRC frames considering infill walls consisted of RCB.

Fig. 16 shows the *P*-Δ curve of bare frame, infilled frame, the frame portion of IF and the masonry portion of IF under different axial load ratio. As being seen from this figure, the stiffness and ductility of all structural parts decrease with the increment of axial load ratio, especially in case of BF. Ultimate bearing strength of IF increases first and then decreases with the increment of axial load ratio, and the descending branch of *P*-Δ curve becomes steep prematurely. However, peak bearing strength and elastic stiffness of the masonry portion of IF change slightly under
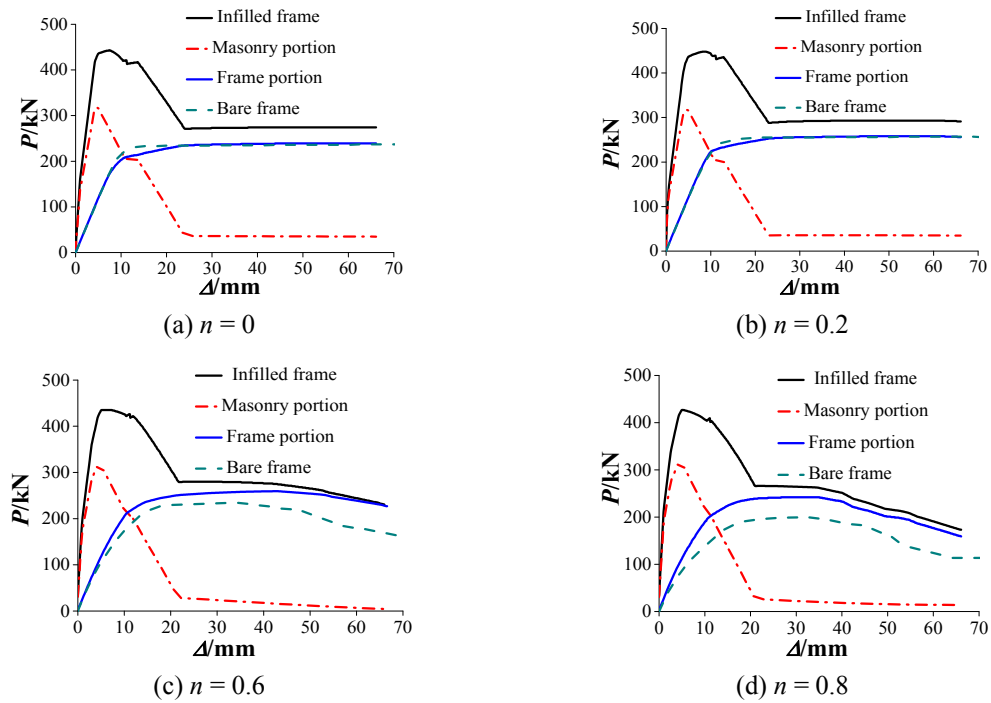
(a) $n = 0$ (b) $n = 0.2$

(c) $n = 0.6$ (d) $n = 0.8$

Fig. 15 Comparison of load-displacement curves under different axial load ratio
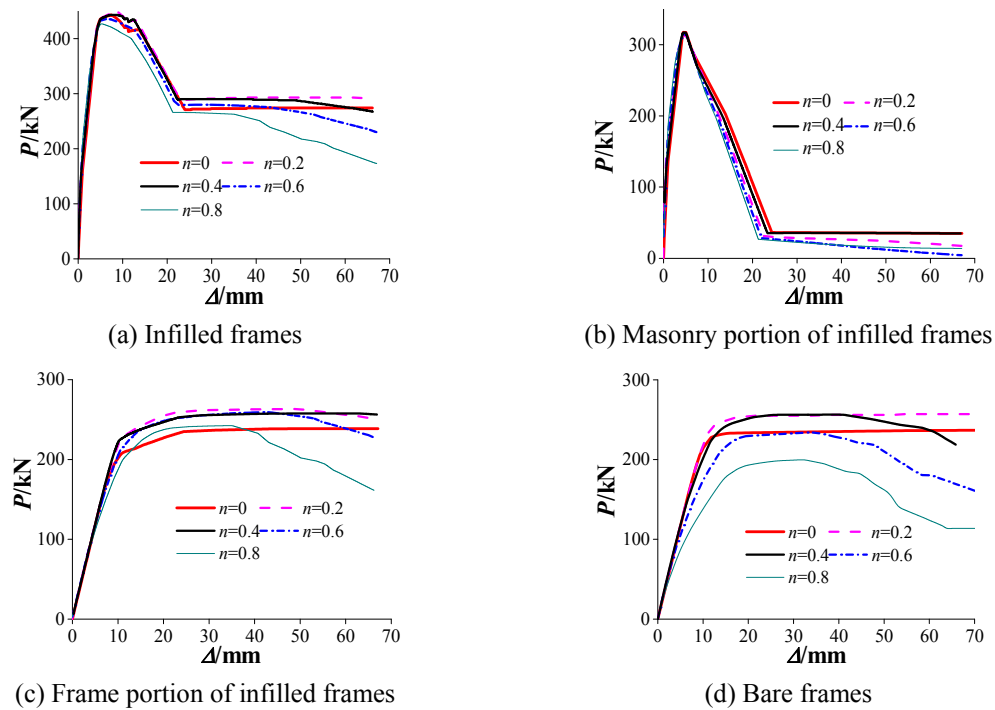
(a) Infilled frames (b) Masonry portion of infilled frames

(c) Frame portion of infilled frames (d) Bare frames

Fig. 16 Load-displacement curves of different portions under different axial load ratio

(a) w = 1.3 (b = 1560, h = 1200 mm)   (b) w = 2.2 (b = 2640, h = 1200 mm)   (c) w = 2.6 (b = 3120, h = 1200 mm)
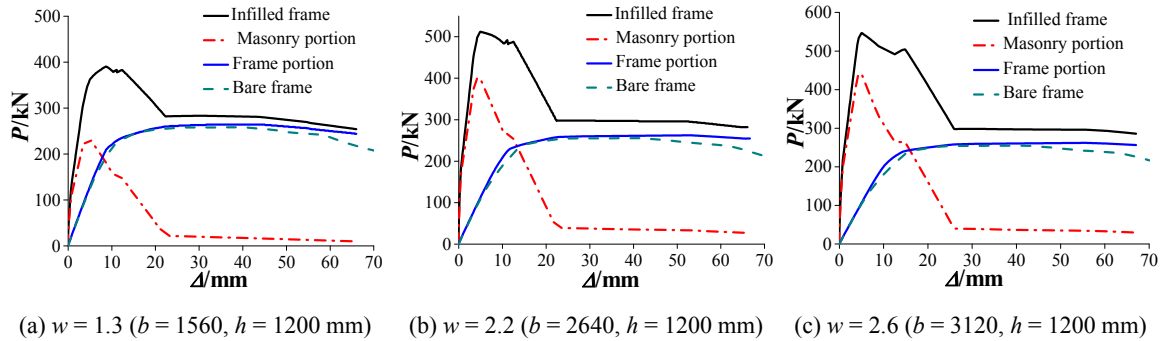
Fig. 17 Comparison of load-displacement curves under different aspect ratio

the influence of axial load ratio. For the frame portion of IF, the P-Δ curves are similar when n is 0.2, 0.4 and 0.6 except 0.8. It should be noted that the stiffness and ductility of BF considerably decrease when axial load ratio reaches 0.6, this finding indicates the vertical load is mainly borne by the frame portion of IF under high axial load ratio. Nevertheless, the plasticity hinges of column bottom of the frame portion of IF are postponed under the effects of infill walls. Therefore, the mechanical performance of the frame portion of IF has improved compared with BF.

6.2 Aspect ratio

In many actual buildings, geometric configurations of masonry walls may be different for structural and architectural reasons. To study the effects of aspect ratio on seismic response of the masonry-SRRC frame, the frames discussed above are re-analyzed when b/h is 1.3, 1.7, 2.2 and 2.6 respectively. The aspect ratio is defined as $w = b/h$, where b stands for the width of wall and h stands for the height of wall.

As being seen from Fig. 17, the P-Δ curves of the frame portion of IF are similar to the one of BF from the numerical analyses with the increment of aspect ratio, indicating that the effects of the masonry of IF acting on the bounding frame keep little change under different aspect ratio. The decreasing interaction between the frame portion and the masonry portion result in large lateral displacement of IF with the increment of aspect ratio. From Fig. 16(c), it is noted that the descending branch of the curve occurs to ascend suddenly and then descend again when b/h reaches 2.6. It is considered that the diagonal strut action caused by masonry portion develops further resistance after the frame-infill interaction weakens and the bearing capacity of the frame portion is still increasing as well.

Fig. 18 shows the bearing capacity and stiffness of IF increase significantly with the increment of aspect ratio, it is mainly caused by the contribution of the masonry portion. On the other hand, the bearing capacity and stiffness of BF and the frame portion of IF change slightly under the influence of aspect ratio.

6.3 Infill thickness

A range of infill thickness from 60 mm to 180 mm at 30 mm intervals was considered in the parametric analysis on its effect on the masonry response in SRRC frames. Fig. 19 shows that the horizontal bearing load of infilled frame increases significantly as the infill thickness increases, but
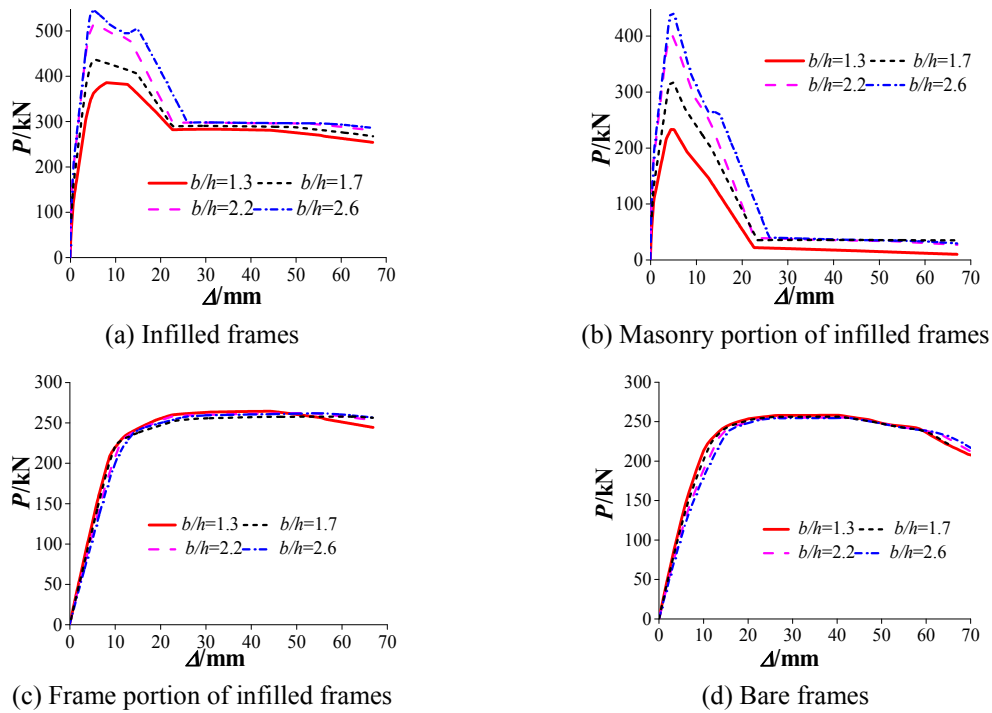
(a) Infilled frames   (b) Masonry portion of infilled frames

(c) Frame portion of infilled frames   (d) Bare frames

Fig. 18 Load-displacement curves of different portions under different aspect ratio

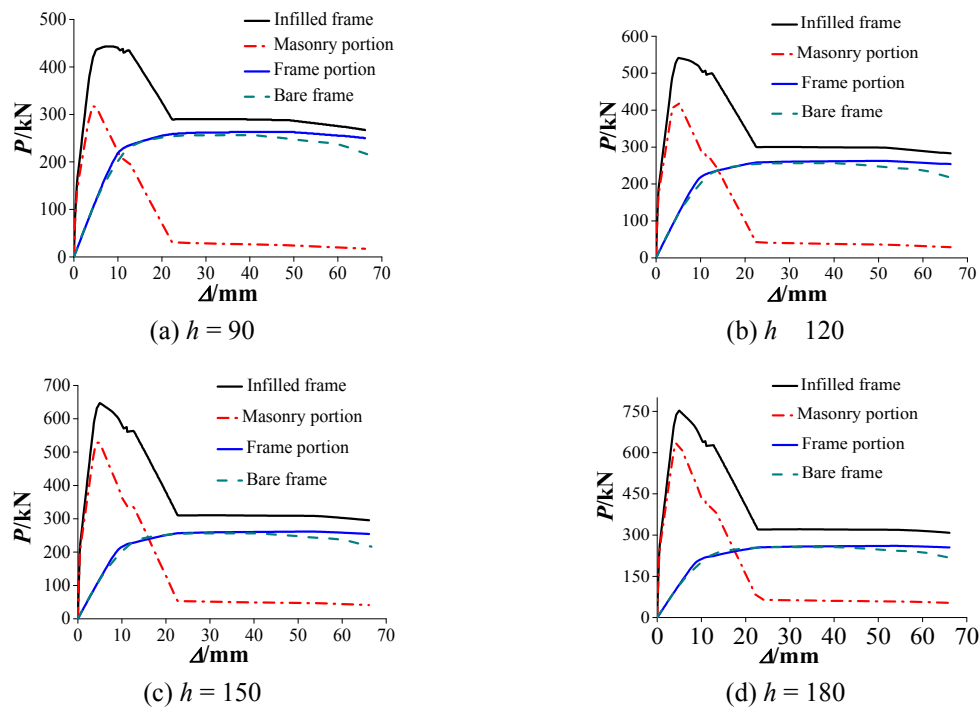(a) *h* = 90   (b) *h*   120

(c) *h* = 150   (d) *h* = 180

Fig. 19 Comparison of load-displacement curves under different infill thickness

the descending branch of *P*-Δ curve of IF becomes steeper, which is similar to that of masonry portion. The figure also illustrates an increase in infill thickness have little effect on frame portion of infilled frames.

Fig. 20 shows the *P*-Δ curve of BF, IF, the frame portion of IF and the masonry portion of IF under different infill thickness. It can be seen that the stiffness and peak strength of infilled frames increase when infill thickness increases, but the bearing strength of masonry portion of IF show little change at the later loading stage. The variations of load with displacement in infilled frames are similar with the masonry portion.

6.4 Steel ratio

The effect of steel ratio on the share of horizontal force of the SRRC frames is investigated for the steel ratio values of 3.32%, 4.19%, 4.98% and 6.05%, corresponding to the sections of I10, I12.6, I14 and I16, respectively. As shown in Fig. 21, horizontal bearing strength of IF increases slowly as the steel ratio increases, the stiffness contribution of masonry portion for IF is still predominant at the early stage of loading. The figure also illustrates an increase in steel ratio have little effect on masonry portion of IF.

Fig. 22 shows the *P*-Δ curve of BF, IF, the frame portion of IF and the masonry portion of IF under steel ratio. As being seen from this figure, the peak strength and ultimate strength of IF
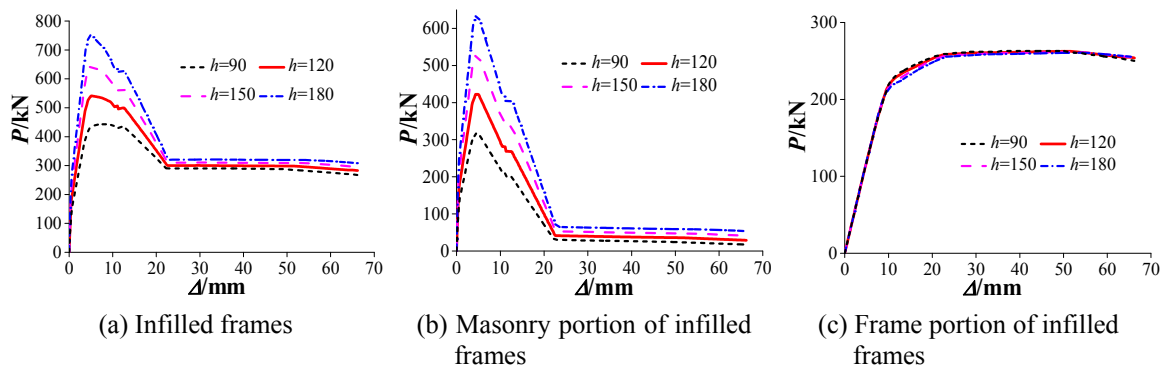

| (a) Infilled frames | (b) Masonry portion of infilled frames | (c) Frame portion of infilled frames |

Fig. 20 Load-displacement curves of different portions under different infill thickness

| (a) ρ_{ss} = 3.32% | (b) ρ_{ss} = 4.19% | (c) ρ_{ss} = 6.05% |

Fig. 21 Comparison of load-displacement curves under different steel ratio

(a) Infilled frames
(b) Masonry portion of infilled frames
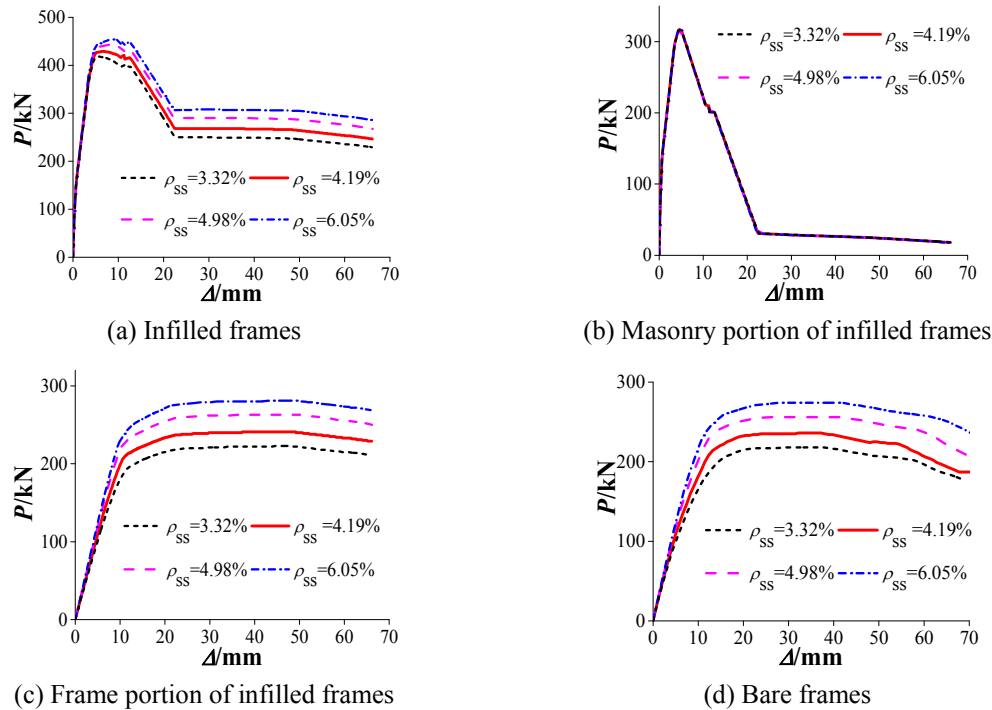(c) Frame portion of infilled frames
(d) Bare frames
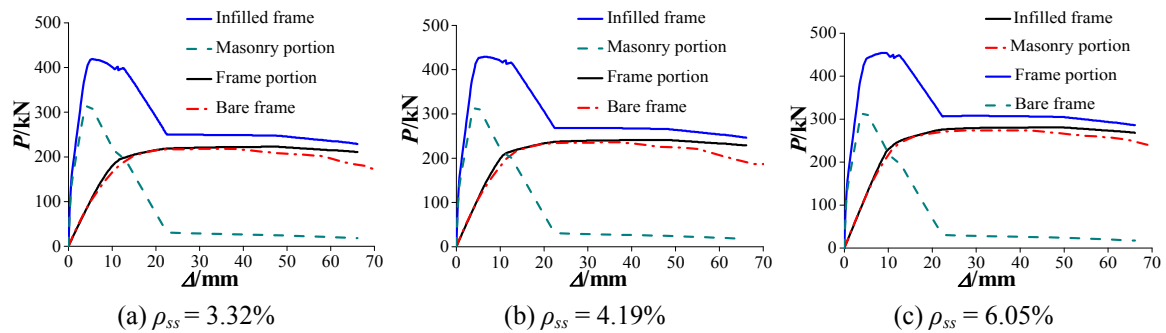
Fig. 22 Load-displacement curves of different portions under different steel ratio

become larger when steel ratio increases, while the ascending curves are identical. The effects of steel ratio on the share of horizontal force supported by the frame portion and the masonry portion are slight. However, a larger steel ratio often affects the concrete area and cannot guarantee the quality of concrete construction. A reasonable steel ratio is essential.

7. Conclusions

The main conclusions drawn from this study are given below:

● Crushing of the mid-height, top left and top right corner of infill wall and horizontal sliding cracks near the mid-height of the wall were observed in S2 under lateral cyclic loading.
● The experimental results showed the infill which consists of RCB increases the initial stiffness of the structure by approximately 12.6 times, and the maximum bearing capacity by approximately 1.75 times. The effects of masonry wall remained effective through numbers of displacement cycles after a drift of 1.2%. Then the lateral load was mainly borne by the SRRC frame portion of S2. However, the partial infill of S3 could not play a role in passive energy dissipation, which increased the initial stiffness of S3 by approximately 2 times.
● The numerical models indicated the mechanical performance of the frame portion of infilled SRRC frames were better than that of the bare SRRC frame under different axial load ratio. The initial stiffness and peak bearing capacity of the masonry potion of the infilled SRRC

frame increased with the increment of aspect ratio significantly, whereas its ductility decreases. A larger steel ratio resulted in an increase in the peak strength and ultimate strength of infilled frames, but does not change the masonry response. An increase in infill thickness mainly enhanced the seismic resistance of masonry portion, but did not change the frame portion.

Acknowledgments

References

Agrawal, R. and Hora, M.S. (2012), "Nonlinear interaction behaviour of infilled frame-isolated footings-soil system subjected to seismic loading", *Struct. Eng. Mech.*, *Int. J.*, **44**(1), 85-107.

Asteris, P.G., Antoniou, S.T. and Sophianopoulos, D.S. (2011), "Mathematical macromodeling of infilled frames: State of the art", *J. Struct. Eng.*, **137**(12), 1508-1517.

Cavaleri, L. and Di Trapani, F. (2014), "Cyclic response of masonry infilled RC frames: Experimental results and simplified modeling", *Soil Dyn. Earth. Eng.*, **65**(7), 224-242.

Dolšek, M. and Fajfar, P. (2008), "The effect of masonry infills on the seismic response of a four-storey reinforced concrete frame — a deterministic assessment", *Eng. Struct.*, **30**(7), 1991-2001.

El-Dakhakhni, W.W., Elgaaly, M. and Hamid, A.A. (2003), "Three-strut model for concrete masonry-infilled steel frames", *J. Struct. Eng.*, **129**(2), 177-185.

Etxeberria, M., Vázquez, E. and Marí, A. (2007), "Influence of amount of recycled coarse aggregates and production process on properties of recycled aggregate concrete", *Cem. Concr. Res.*, **37**(5), 735-742.

Gomes, M. and de Brito, J. (2009), "Structural concrete with incorporation of coarse recycled concrete and ceramic aggregates: Durability performance", *Mater. Struct.*, **42**(5), 663-675.

Hashemi, S.A. (2007), "Seismic evaluation of reinforced concrete building including effects of masonry infill walls", Ph.D. Dissertation; University of California, Berkeley, CA, USA.

Koutromanos, I., Stavridis, A. and Shing, P.B. (2011), "Numerical modeling of masonry-infilled RC frames subjected to seismic loads", *Com. Struct.*, **89**(11), 1026-1037.

Liu, Z.Q., Xue, J.Y. and Ma, H. (2015), "Testing and numerical simulation of the normal cross-section bearing capacity of steel reinforced recycled concrete columns", *Eng. Mech.*, **32**(1), 81-87.

Lubliner, J. (2006), *Plasticity Theory*, Pearson Education, Upper Saddle River, NJ, USA.

Ma, H., Xue, J.Y. and Zhang, X.C. (2013), "Seismic performance of steel-reinforced recycled concrete columns under low cyclic loads", *Constr. Build. Mater.*, **48**, 229-237.

Mander, J.B., Priestley, M.J.N. and Park, R. (1988), "Theoretical stress-strain model for confined concrete", *J. Struct. Eng.*, **114**(8), 1804-1826.

Otsuki, N., Miyazato, S. and Yodsudjai, W. (2003), "Influence of recycled aggregate on interfacial transition zone, strength, chloride penetration and carbonation of concrete", *J. Mater. Civil Eng.*, **15**(5), 443-451.

Poon, C.S., Kou, S.C. and Lam, L. (2002), "Use of recycled aggregates in molded concrete bricks and blocks", *Constr. Build. Mater.*, **16**(5), 281-289.

Pujol, S. and Fick, D. (2010), "The test of a full-scale three-story RC structure with masonry infill walls", *Eng. Struct.*, **32**(10), 3112-3121.

Smyrou, E., Blandon, C. and Antoniou, S. (2011), "Implementation and verification of a masonry panel model for nonlinear dynamic analysis of infilled RC frames", *Bull. Earthq. Eng.*, **9**(6), 1519-1534.

Tasnimi, A.A. and Mohebkhah, A. (2011), "Investigation on the behavior of brick-infilled steel frames with openings, experimental and analytical approaches", *Eng. Struct.*, **33**(3), 968-980.

Xiao, J.Z. (2008), *Recycled Concrete*, Architecture and Building Press, Beijing, China.

Xue, J.Y., Bao, Y.Z. and Ren, R. (2014), "Experimental study on seismic performance of steel reinforced recycled concrete inner-frame joints under low-cyclic reversed loading", *China Civ. Eng. J.*, **47**(10), 1-8.

CC